Inertial Navigation aided by Ultra-Wideband Ranging for Ship Docking and Harbor Maneuvering

Håkon Hagen Helgesen, Torbjørn Fuglestad, Krzysztof Cisek, Bjørnar Vik, Øivind Kåre Kjerstad and Tor Arne Johansen

Abstract

This paper presents an inertial navigation system aided by local ranging measurements derived from an ultra-wideband system. The system consists of one onboard tag and several onshore anchors. It is motivated by the need to complement satellite systems in harbor areas to reduce the risk of localization dropout during high precision closed-loop maneuvering and docking of ships as it may imply severe consequences. The proposed state estimation algorithm includes ranging bias to compensate for minor inaccuracies originating mostly from tag and anchor processing time. The complete ultra-wideband aided inertial navigation system is validated using full-scale measurements collected during multiple dockings of a passenger ferry in Trondheim, Norway. The results show that the proposed localization system has comparable performance to state-of-the art inertial navigation systems aided by real-time kinematic satellite position measurements. Thus, it offers a viable alternative and complement which may contribute to safe and efficient high precision closed-loop maneuvering and docking of marine vessels.

Index Terms

Inertial Navigation, Ultra-wideband ranging, Docking and Localization

I. Introduction

State-of-the-art navigation systems for ships use an inertial navigation system (INS) fused with measurements from a global navigation satellite system (GNSS). The positioning solution obtained with GNSS and INS is considered to be accurate enough in most applications, both in maritime environments [1] and on land [2]. However, loss of GNSS measurements occurs, and is often a critical single point of failure. Harbors and narrow fjords are examples of locations where GNSS measurements may be unavailable or inaccurate. GNSS signals are also prone to interference from electromagnetic fields or deliberate attempts to misguide the receiver through jamming and spoofing [3]–[5].

Håkon Hagen Helgesen, Torbjørn Fuglestad and Tor Arne Johansen are with the NTNU Centre for Autonomous Marine Operations and Systems, Department of Engineering Cybernetics, Norwegian University of Science and Technology

Bjørnar Vik is with Kongsberg Maritime AS, Aalesund, Norway.

Øivind Kåre Kjerstad is with Department of Ocean Operations and Civil Engineering at NTNU, Aalesund, Norway.

Krzysztof Cisek is with Scout Drone Inspection, Trondheim, Norway.

Moreover, the robustness of augmented GNSS services, such as real-time kinematic (RTK) GNSS or precise point positioning (PPP) [6], is questionable, particularly in urban areas due to multipath and other undesirable effects [7]. These GNSS errors are often systematic and induce colored noise that reduce the accuracy. The increased cost, convergence time and infrastructure on land are additional drawbacks for augmented GNSS services. Issues caused by signal degradation and outage can be reduced through fault detection as described in [8], but there are still many challenges with the use of GNSS in safety-critical systems with strong requirements to accuracy and uptime.

The GNSS challenges is a potential showstopper for the development of ship systems with strong requirements to safety, robustness, and reliability. A relevant example is development of automatic steering systems for ships in harbor maneuvering and docking. Steering systems require accurate feedback from the navigation states to calculate suitable control forces from the actuators. Development of automatic steering systems is desirable to reduce the stress level of human operators. Docking and harbor maneuvering are particularly stressful and complex tasks due to varying environmental conditions and dynamic scenery. Moreover, automatic steering is a key component for future applications such as autonomous transport of passengers and cargo, and automated unloading and loading. These applications cannot be realized without a reliable localization system with the required redundancy level. Therefore, it is necessary to investigate sensor technologies and algorithms for ship navigation systems.

Navigation systems for surface ships are most often based on a position reference system and a heading reference. A relevant example is a localization system based on GNSS and a gyrocompass. Another strategy is inertial navigation systems (INS) used mostly for underwater vehicles in maritime environments. INS employ an inertial measurement unit (IMU) to predict the vehicle motion [9]. A pure INS without aiding measurements is prone to significant drift, and the drift increases at least linearly in time [10]. Therefore, INS has more recently been combined with GNSS and a heading reference to combine the advantages of both approaches. The high-frequency INS can give estimates rapidly and aiding sensors ensure that drift is avoided. A third approach is model-based navigation systems. A model-based navigation system require measurements and/or estimates of forces from propulsion, steering and the environment such as wind, waves and current to predict the motion of the ship [11]. They are mostly used in dynamic positioning systems where low-speed assumptions can be included in the models. Common for all strategies is the need for aiding measurements during high-precision maneuvering.

Several sensor technologies have been explored for aiding of ships and other vehicles. Optical sensors have performed well in several applications using algorithms based on simultaneous localization and mapping (SLAM) [12], [13]. Visual sensors have also been used in underwater docking applications [14], which share many of the challenges faced in GNSS-denied environments [15]–[17]. Optical sensors are cheap and versatile but struggle in poor weather and illumination conditions. Consequently, they cannot be used as an alternative to GNSS in a robust manner. SLAM or visual odometry can also be applied using LIDARs [18]. LIDARs are often more robust with respect to environmental conditions but have a short localization range, often below $100\,\mathrm{m}$. LIDARs with better range are expensive, and the memory and processing requirements are also troublesome, especially for real-time applications. State-of-the-art SLAM algorithms need to solve the long- and short-term data association problem which in case of failure is critical and can cause large errors in the localization accuracy. Moreover, the harbor environment is dynamic with moving scenery, which breaks the assumptions in the most proven SLAM frameworks

[19]. Conventional position reference systems used on ships include radio, radar, laser, taut wire, and hydro-acoustic systems, but are not suitable for harbor areas, expensive or do not have the necessary robustness and accuracy.

This paper investigates ultra-wideband (UWB) ranging for aiding of ships in harbor maneuvering. UWB signals are used to measure the range between a tag and several anchors in the operating area [20], [21]. The analogy to GNSS is clear; the tag is the receiver on-board the vehicle and the anchors correspond to GNSS satellites. An obstacle-free line of sight between the anchor and tag is necessary to obtain ranging measurements. Obstacles along the line of sight can both block the signal and degrade the accuracy through multipath. The ranging measurement is often based on the time a signal uses to travel from the tag to the anchor and back (or another time-of-flight scheme). The UWB signal is transmitted on a wide frequency band, which mitigates the most severe effects of multipath and provides good spatial resolution [22]. Commercially available UWB ranging systems specify an accuracy at decimeter level. These systems typically have a maximum measurement range of a few hundred meters, which should provide sufficient aiding for harbor maneuvering. The maximum range depends on the chosen transmission frequency and the signal strength required to accept the incoming signal. UWB ranging systems are not affected significantly by weather conditions, and it is a cost-effective system when combined with low-cost MEMS IMUs.

UWB ranging systems have been used for localization previously but existing work focus mostly on indoor localization systems [21]. Some outdoor examples exist, such as localization for unmanned aerial vehicles [23]–[27]. However, most works have not systematically investigated calibration and estimation of UWB sensor bias, calibration of anchor position, or used a comprehensive amount of experimental data to validate their work. This paper investigates these aspects and shows the entire pipeline from design of a localization system to experimental verification of the system, including calibration of anchor positions and biases.

A. *Scope of work & Outline*

This paper presents a localization system using an IMU fused with UWB ranging measurements. More specifically, how ships can use UWB ranging for aiding in harbors are investigated. This includes estimation of the 6-DOF motion of a ship. Moreover, estimation of sensor bias and calibration procedures needed for identification of anchor positions are studied thoroughly. The localization system is based on the error-state formulation of the extended Kalman filter (EKF). Attitude is parameterized by the unit quaternion, which leads to a solution known as the multiplicative extended Kalman filter (MEKF) [11]. The UWB ranging measurements are fused with the IMU measurements in a tightly-coupled system. A tightly-coupled system is preferred since loosely-coupled systems based on multilateration require at least three ranging measurements simultaneously. The tight coupling ensures that each available ranging measurement is utilized, which is valuable when only a single anchor has an obstacle-free line of sight to the tag. The proposed system is compared with a state-of-the-art solution using RTK GNSS fused with IMU measurements. A comprehensive amount of full-scale field experimental data from several ferry dockings is used for validation. Even though an INS is used as showcase, UWB ranging can obviously be used for aiding in other navigation systems.

The paper is structured in the following manner. Section II presents the coordinate frames and the mathematical notation used in this paper. Section III presents the assumed sensor technologies and the corresponding measurement principles. The localization system is presented in Section IV where the MEKF is described in detail. The experimental design and calibration procedures are described in Section V. Full scale experimental results are presented in Section VI before the paper is concluded in Section VII.

II. Preliminaries

This section serves as an introduction to the notation and definitions used throughout this paper.

A. Notation

The following list summarizes the most important quantities in this paper:

$\mathbf{I}_n$	Identity matrix of size $n \times n$
$(.)^\top$	Vector and matrix transpose
$\{\mathrm{b}\}$	Vehicle body-fixed coordinate frame
$\{\mathrm{n}\}$	North-east-down (NED) reference frame
$\{m_i\}$	IMU measurement frame
$\{m_g\}$	GNSS measurement frame
$\mathbf{p}$	Vectors are bold with small letter
$\mathbf{A}$	Matrices are bold with capital letter
$\mathbf{p}_{nb}^n$	Vector $\mathbf{p}$ describing frame $\{\mathrm{b}\}$ relative to $\{\mathrm{n}\}$ decomposed in $\{\mathrm{n}\}$
$\mathbf{R}_b^n$	Rotation matrix transforming a vector from $\{\mathrm{b}\}$ to $\{\mathrm{n}\}$, $\in SO(3)$
$\mathbf{S}(\mathbf{a})$	Skew-symmetric matrix of vector $\mathbf{a}$ used for cross products, $\in SS(3)$
$\boldsymbol{\Theta}$	Vector of Euler angles
$\mathbf{q}_b^n$	Unit quaternion representation of attitude (rotation from $\{\mathrm{b}\}$ to $\{\mathrm{n}\}$)
$\mathbf{q}_1 \otimes \mathbf{q}_2$	Quaternion product using the Hamiltonian representation
ϕ	Roll angle
θ	Pitch angle
ψ	Yaw/heading angle
$\boldsymbol{\omega}_{nb}^b$	Angular velocity of $\{\mathrm{b}\}$ relative to $\{\mathrm{n}\}$ decomposed in $\{\mathrm{b}\}$
$\mathbf{f}_{nb}^b$	Specific force of $\{\mathrm{b}\}$ relative to $\{\mathrm{n}\}$ decomposed in $\{\mathrm{b}\}$

B. Coordinate Frames

Several coordinate frames are employed in this research. The north-east-down (NED) frame $\{\mathrm{n}\}$ is a local tangent plane used for navigation and considered to be inertial locally. The rotation of the Earth is neglected in NED and the tangent plane has an inherent flat-earth assumption making it accurate only in a small local area [11]. The x axis of $\{\mathrm{n}\}$ points towards the true geographic north, the y axis towards east, and the z axis down to complete the right-handed system. The body-fixed frame is a vehicle frame denoted $\{\mathrm{b}\}$, which moves with the vehicle. Its origin is a fixed point on the vehicle, most often close to the center of gravity (it is a design choice). The x axis points to along the forward direction of the vehicle, the y axis to starboard and the z axis points downwards. Other reference frames of interest are the sensor frames in which different sensors are aligned. Each sensor has its own right-handed frame that can be related to the body-fixed frame through calibration (rotation and lever arm compensation).

C. Attitude Parameterization and Kinematics

Representation of attitude requires at least three parameters. However, it is not possible to represent attitude globally without a singularity when using the minimal number of parameters [28]. Unit quaternions are global and singularity free at the cost of one additional parameter and double cover of SO(3).

Three attitude representations are used in this paper. Euler angles are used for visualization of the results. A unit quaternion using the Hamiltonian representation is used to represent attitude in the inertial navigation problem. The attitude error in the inertial navigation problem is represented using the four times Modified Rodrigues Parameters (MRP). The reasoning behind these choices is well known and discussed later. The rotation between two frames $\{\mathrm{a}\}$ and $\{\mathrm{b}\}$ can be described by the unit quaternion

$$\mathbf{q}_b^a = \begin{pmatrix} \eta \\ \boldsymbol{\epsilon} \end{pmatrix} = \begin{pmatrix} \eta \\ \epsilon_1 \\ \epsilon_2 \\ \epsilon_3 \end{pmatrix} \in \mathbb{Q} \tag{1}$$

where $\mathbb{Q}$ is the set of unit quaternions defined in [11]. η is the scalar part of the quaternion and $\boldsymbol{\epsilon}$ is the vector part of the quaternion. A rotation matrix representing the same rotation is

$$\mathbf{R}_b^a := \mathbf{I}_3 + 2\eta\mathbf{S}(\boldsymbol{\epsilon}) + 2\mathbf{S}^2(\boldsymbol{\epsilon}) \tag{2}$$

The quaternion product is used for compositions of rotations and defined as

$$\mathbf{q}_3 = \mathbf{q}_1 \otimes \mathbf{q}_2 = \begin{bmatrix} \eta_{q_1}\eta_{q_2} - \boldsymbol{\epsilon}_{q1}^\top \boldsymbol{\epsilon}_{q2} \\ \eta_{q_1}\boldsymbol{\epsilon}_{q2} + \eta_{q_2}\boldsymbol{\epsilon}_{q1} + \mathbf{S}(\boldsymbol{\epsilon}_{q1})\boldsymbol{\epsilon}_{q2} \end{bmatrix} \tag{3}$$

The angular rate of the vehicle $\boldsymbol{\omega}_{nb}^b$ is related to the attitude $\mathbf{q}_b^n$ through the kinematic equation

$$\dot{\mathbf{q}}_b^n = \frac{1}{2}\mathbf{q}_b^n \otimes \bar{\boldsymbol{\omega}}_{nb}^b = \frac{1}{2}\boldsymbol{\Omega}(\boldsymbol{\omega}_{nb}^b)\mathbf{q}_b^n \tag{4}$$

where $\bar{\boldsymbol{\omega}}_{nb}^b = [0, \boldsymbol{\omega}_{nb}^b]^\top$ and the operator $\boldsymbol{\Omega}$ is

$$\boldsymbol{\Omega}(\boldsymbol{\omega}_{nb}^b) = \begin{bmatrix} 0 & -(\boldsymbol{\omega}_{nb}^b)^\top \\ \boldsymbol{\omega}_{nb}^b & -\mathbf{S}(\boldsymbol{\omega}_{nb}^b) \end{bmatrix} \tag{5}$$

The kinematic equations for the position and velocity are simply

$$\begin{aligned}\dot{\mathbf{p}}^n_{nb} &= \mathbf{v}^n_{nb} \\ \dot{\mathbf{v}}^n_{nb} &= \mathbf{a}^n_{nb}\end{aligned} \tag{6}$$

where $\mathbf{p}^n_{nb}, \mathbf{v}^n_{nb}$ and $\mathbf{a}^n_{nb}$ are the vehicle position, velocity and acceleration, respectively, decomposed in the $\{\mathrm{n}\}$ frame.

D. Navigation states

The pose of a ship in 6 degrees of freedom (DOF) is typically represented by the position, velocity, and attitude of the ship. Nine or ten elements are needed to represent these states depending on the choice of attitude representation. In addition, inertial sensor bias is most often included as additional states since these states must be estimated in real time or through a static calibration before the mission.

III. Sensor Models

Three main sensors are used to estimate the navigation states of the ship in this paper. An inertial measurement unit is used to measure acceleration (specific force) and angular rate. The UWB ranging system is used to measure the range between a tag on the ship and several anchors placed in the docking area. In addition, two RTK-GNSS receivers with separate antennas are used as a reference (ground truth).

A. Inertial Measurement Unit (IMU)

The IMU is mounted in a known location in the body frame. The IMU frame is denoted $\{m_i\}$. The origin of $\{m_i\}$ has a lever arm to the origin of $\{\mathrm{b}\}$ but the axes of $\{m_i\}$ are assumed to be aligned with the axes of $\{\mathrm{b}\}$ through careful installation and calibration of the IMU. The three-axis angular rate measurement is assumed to obey the following sensor model

$$\begin{aligned}\boldsymbol{\omega}^b_{\text{imu}} &= \boldsymbol{\omega}^b_{nb} + \mathbf{b}^b_{\text{ars}} + \mathbf{w}^b_{\text{ars}} \\ \dot{\mathbf{b}}^b_{\text{ars}} &= \mathbf{w}^b_{b,\text{ars}}\end{aligned} \tag{7}$$

where the bias vector is denoted $\mathbf{b}^b_{\text{ars}}$, and $\mathbf{w}^b_{\text{ars}}$ and $\mathbf{w}^b_{b,\text{ars}}$ are white noise processes representing measurement and bias noise, respectively. $\boldsymbol{\omega}^b_{\text{imu}}$ is the angular rate measurement vector and $\boldsymbol{\omega}^b_{nb}$ is the true angular rate of the vehicle with respect to $\{\mathrm{n}\}$ decomposed in $\{\mathrm{b}\}$. Note that the angular velocity of any point on the body is assumed to be equal through the rigid-body assumption so it is not necessary to relate the measurement to the IMU frame.

The three-axis specific force measurement is denoted $\boldsymbol{f}^b_{\text{imu}}$ and is assumed to obey the following sensor model

$$\begin{aligned}\boldsymbol{f}^b_{\text{imu}} &= (\mathbf{R}^n_b)^\top(\mathbf{a}^n_{nm_i} - \mathbf{g}^n) + \mathbf{b}^b_{\text{acc}} + \mathbf{w}^b_{\text{acc}} \\ \dot{\mathbf{b}}^b_{\text{acc}} &= \mathbf{w}^b_{b,\text{acc}}\end{aligned} \tag{8}$$

where the accelerometer bias is denoted $\mathbf{b}^b_{\text{acc}}$, and $\mathbf{w}^b_{\text{acc}}$ and $\mathbf{w}^b_{b,\text{acc}}$ are white noise processes modeling the measurement and bias noise, respectively. $\mathbf{g}^n$ is the gravity vector decomposed in $\{\mathrm{n}\}$ and $\mathbf{a}^n_{nm_i}$ is the acceleration of $\{m_i\}$ with respect to $\{\mathrm{n}\}$ decomposed in $\{\mathrm{n}\}$.

B. Ultra-Wideband Ranging System

The UWB ranging system can provide measurements in two separate ways. One possibility is to treat each ranging measurement between the tag and anchor as an independent measurement. This becomes a tightly-coupled system when fused with the IMU. Alternatively, multiple ranging measurements from the same time instant can be used to solve a multilateration problem and create a 3-DOF position measurement [29]. The latter choice requires at least three independent time-synchronized range measurements to obtain the 3D-position and an additional measurement if a common bias is present. This leads to a loosely-coupled system. Due to the limited number of available UWB anchors, it is beneficial to treat each ranging measurement independently. A single range measurement can provide valuable aiding of an INS.

A single ranging measurement r_{ti} between the tag *t* and anchor *i* is expressed mathematically as

$$r_{ti} = ||\mathbf{p}^n_{nt} - \mathbf{p}^n_{na_i}||_2 \tag{9}$$

where $\mathbf{p}^n_{nt}$ is the unknown tag position and $\mathbf{p}^n_{na_i}$ is the known location of anchor *i*. The state of interest is the position of the ship (body frame), namely $\mathbf{p}^n_{nb}$. Consequently, the lever arm between the body frame and tag must be included. Moreover, it is assumed that the system has a common measurement bias for all anchors. This bias represents the processing time in the tag. It is assumed that the UWB system measures round-trip time of flight to remove the clock difference between the anchors and the tag. Therefore, a common bias is sufficient to represent the delay caused by processing time. Considering all these aspects, the measurement model becomes

$$r_{ti} = ||\mathbf{p}^n_{nb} + \mathbf{R}^n_b \mathbf{p}^b_{bt} - \mathbf{p}^n_{na_i}||_2 + b_{\text{uwb}} + w_{\text{uwb}_i} \tag{10}$$

where $\mathbf{p}^b_{bt}$ is the lever arm between the tag antenna and the origin of $\{\text{b}\}$ decomposed in $\{\text{b}\}$. b_{uwb} and w_{uwb_i} are the bias and measurement noise from anchor i, respectively.

C. Global Navigation Satellite System

GNSS is used for comparison, calibration and initialization only. Scenarios where GNSS is available during the initial phase of the docking operation, but will become unavailable during the final and most critical phase, are considered. A common model for the GNSS measurement is chosen. It is assumed that measurements with centimeter precision is available through carrier-phase measurements (RTK). Systematic errors from GNSS are assumed to be corrected in the RTK processing and the measurement noise is therefore assumed to be additive and white. The chosen GNSS measurement model is

$$\begin{aligned} \mathbf{p}^n_{\text{gnss}} &= \mathbf{p}^n_{nm_g} + \mathbf{w}^n_{\text{gnss}} \\ &= \mathbf{p}^n_{nb} + \mathbf{R}^n_b \mathbf{p}^b_{bm_g} + \mathbf{w}^n_{\text{gnss}} \end{aligned} \tag{11}$$

where $\mathbf{p}^n_{\text{gnss}}$ is the position measurement and $\mathbf{w}^n_{\text{gnss}}$ is white noise. $\mathbf{p}^b_{bm_g}$ is the lever arm between the origin of $\{\text{b}\}$ and the GNSS antenna position decomposed in $\{\text{b}\}$. Two different lever arms are obviously present in a dual-antenna design.

IV. Error-state Kalman Filter (ESKF)

This chapter describes the localization (ESKF) algorithm in detail. That includes the design of an error-state MEKF that is used for aided INS. Section IV-A reviews the fundamental idea in the ESKF. Section IV-B describes the strapdown equations and how inertial measurements are used to predict high-frequency state estimates in a dead reckoning fashion. The measurement equations used for feedback and reset of the error states are presented in Section IV-C. Finally, practical aspects related to design choices and implementation are described in Section IV-D

A. Fundamentals of the ESKF

The indirect feedback filter design is used in this paper [11]. The fundamental idea is to estimate the true state as a combination of an IMU-driven nominal state and aiding by localization measurements to correct the error of the corresponding nominal state. The true state $\mathbf{x}$ is described mathematically as

$$\mathbf{x} = \hat{\mathbf{x}} \oplus \delta\mathbf{x} \tag{12}$$

where $\hat{\mathbf{x}}$ is the nominal (predicted) state and $\delta\mathbf{x}$ is the error state. The generic composition $\oplus$ is used since injection of the attitude error is not a regular arithmetic addition. The nominal state is predicted through the strapdown equations. The error states are corrected using the aiding measurement equations. The error states are injected into the nominal states whenever a new aiding measurement is available. After the injection, the error states are reset to zero since the information is transferred to the nominal states. The nominal state vector is

$$\mathbf{x} = \begin{bmatrix} \mathbf{p}_{nb}^{n}, & \mathbf{v}_{nb}^{n}, & \mathbf{q}_{b}^{n}, & \mathbf{b}_{\text{acc}}^{b}, & \mathbf{b}_{\text{ars}}^{b}, & b_{\text{uwb}} \end{bmatrix}^{\top} \tag{13}$$

which includes NED positions ($\mathbf{p}_{nb}^{n}$), NED velocities ($\mathbf{v}_{nb}^{n}$), attitude represented by the unit quaternion ($\mathbf{q}_{b}^{n}$), accelerometer bias ($\mathbf{b}_{\text{acc}}^{b}$), angular rate bias ($\mathbf{b}_{\text{ars}}^{b}$), and UWB ranging bias (b_{uwb}). The error state vector is

$$\delta\mathbf{x} = \begin{bmatrix} \delta\mathbf{p}, & \delta\mathbf{v}, & \delta\mathbf{a}, & \delta\mathbf{b}_{\text{acc}}, & \delta\mathbf{b}_{\text{ars}}, & \delta b_{\text{uwb}} \end{bmatrix}^{\top} \tag{14}$$

where each state in the nominal state vector has a corresponding error state. The superscripts and subscripts are not used for the error states since these are relative to the nominal states. The attitude error state is represented by $\delta\mathbf{a}$, which is the four-time modified MRP [30] which is a minimal representation of attitude. This parameterization is used to avoid singularities in the covariance matrix, which is the core idea in the MEKF. Consequently, the error state has one element less than the nominal state vector. $\delta\mathbf{a}$ has a singularity at 2π which is acceptable for ships. The nominal state is represented by the unit quaternion to have a global singularity-free representation of attitude.

B. Nominal State Equations

The state kinematics is based on (4) and (6), and familiar Gauss-Markov processes for the bias models:

$$
\begin{aligned}
\dot{\mathbf{p}}^n_{nb} &= \mathbf{v}^n_{nb} \\
\dot{\mathbf{v}}^n_{nb} &= \mathbf{a}^n_{nb} \\
\dot{\mathbf{q}}^n_b &= \frac{1}{2}\boldsymbol{\Omega}(\boldsymbol{\omega}^b_{nb})\mathbf{q}^n_b \\
\dot{\mathbf{b}}^b_{\text{acc}} &= -\mathbf{T}^{-1}_{\text{acc}}\mathbf{b}^b_{\text{acc}} + \mathbf{w}^b_{\text{b, acc}} \\
\dot{\mathbf{b}}^b_{\text{ars}} &= -\mathbf{T}^{-1}_{\text{ars}}\mathbf{b}^b_{\text{ars}} + \mathbf{w}^b_{\text{b, ars}} \\
\dot{b}_{\text{uwb}} &= -t^{-1}_{\text{uwb}}b_{\text{uwb}} + w_{\text{b, uwb}}
\end{aligned} \tag{15}
$$

The nominal state equations are based on the exact kinematics and the IMU sensor models in (7) and (8). For simplicity, it is assumed that the IMU frame coincides with the body frame although the equations can be generalized to handle lever arms between the IMU and the origin of body as described in [11]. The nominal state equations are

$$
\begin{aligned}
\dot{\hat{\mathbf{p}}}^n_{nb} &= \hat{\mathbf{v}}^n_{nb} \\
\dot{\hat{\mathbf{v}}}^n_{nb} &= \hat{\mathbf{R}}^n_b(\mathbf{f}^b_{\text{imu}} - \hat{\mathbf{b}}^b_{\text{acc}}) + \mathbf{g}^n \\
\dot{\hat{\mathbf{q}}}^n_b &= \frac{1}{2}\boldsymbol{\Omega}(\boldsymbol{\omega}_{\text{imu}} - \hat{\mathbf{b}}^b_{\text{ars}})\hat{\mathbf{q}}^n_b \\
\dot{\hat{\mathbf{b}}}^b_{\text{acc}} &= -\mathbf{T}^{-1}_{\text{acc}}\hat{\mathbf{b}}^b_{\text{acc}} \\
\dot{\hat{\mathbf{b}}}^b_{\text{ars}} &= -\mathbf{T}^{-1}_{\text{ars}}\hat{\mathbf{b}}^b_{\text{ars}} \\
\dot{\hat{b}}_{\text{uwb}} &= -t^{-1}_{\text{uwb}}\hat{b}_{\text{uwb}}
\end{aligned} \tag{16}
$$

where the unknown noise terms in (15) are neglected. These equations are based on dead reckoning and is mechanized in discrete time using a first-order integration in this work.

C. Error-State Equations

The error states are used to calculate the covariance of the states and to correct the nominal states. They have an a-priori assumption of being zero. The values of these states are only corrected when aiding measurements are available. The kinematic model for the error states is (neglecting noise terms) [31]

$$
\begin{aligned}
\delta\dot{\mathbf{p}} &= \delta\mathbf{v} \\
\delta\dot{\mathbf{v}} &= -\mathbf{R}(\hat{\mathbf{q}})(\mathbf{S}(\mathbf{f}^b_{\text{imu}} - \hat{\mathbf{b}}_{\text{acc}})\delta\mathbf{a} + \delta\mathbf{b}_{\text{acc}}) \\
\delta\dot{\mathbf{a}} &= -\mathbf{S}(\boldsymbol{\omega}^b_{\text{imu}} - \hat{\mathbf{b}}_{\text{ars}})\delta\mathbf{a} - \delta\mathbf{b}_{\text{ars}} \\
\delta\dot{\mathbf{b}}_{\text{acc}} &= -\mathbf{T}^{-1}_{\text{acc}}\delta\mathbf{b}_{\text{acc}} \\
\delta\dot{\mathbf{b}}_{\text{ars}} &= -\mathbf{T}^{-1}_{\text{ars}}\delta\mathbf{b}_{\text{ars}} \\
\delta\dot{b}_{\text{uwb}} &= -t^{-1}_{\text{uwb}}\delta b_{\text{uwb}}
\end{aligned} \tag{17}
$$

where the relationship $\mathbf{x} = \hat{\mathbf{x}} \otimes \delta\mathbf{x}$ is differentiated to find the error states. The details of the calculations are presented in [31].

The error states are corrected through measurements from UWB. The Jacobian of the measurement model in (10) must be calculated during the correction step of the MEKF. Moreover, the Jacobian is calculated with respect to the error states. Consequently, it is necessary to rewrite (10) as a function of the error states:

$$
\begin{aligned}
r_i =& ||(\mathbf{p}_{nb}^n + \mathbf{R}_b^n \mathbf{p}_{bt}^b - \mathbf{p}_{a_i}^n)||_2 + b_{\text{uwb}} + w_{\text{uwb}_i} \\
=& || \underbrace{(\hat{\mathbf{p}}_{nb}^n + \delta\mathbf{p})}_{\mathbf{p}_{nb}^n} + \underbrace{\hat{\mathbf{R}}_b^n(\mathbf{I}_3 + \mathbf{S}(\delta\mathbf{a}))}_{\mathbf{R}_b^n} \mathbf{p}_{bt}^b - \mathbf{p}_{a_i}^n ||_2 \\
& + \underbrace{(\hat{b}_{\text{uwb}} + \delta b_{\text{uwb}})}_{b_{\text{uwb}}} + w_{\text{uwb}_i} \\
=& || \underbrace{(\hat{\mathbf{p}}_{nb}^n + \delta\mathbf{p}) + \hat{\mathbf{R}}_b^n \mathbf{p}_{bt}^b - \hat{\mathbf{R}}_b^n \mathbf{S}(\mathbf{p}_{bt}^b))\delta\mathbf{a} - \mathbf{p}_{a_i}^n}_{\mathbf{f}(\mathbf{x})} ||_2 \\
& + (\hat{b}_{\text{uwb}} + \delta b_{\text{uwb}}) + w_{\text{uwb}_i} \\
=& ||\mathbf{f}(\mathbf{x})||_2 + (\hat{b}_{\text{uwb}} + \delta b_{\text{uwb}}) + w_{\text{uwb}_i}
\end{aligned}
\tag{18}
$$

The Jacobian of (18) with respect to the error states for a single UWB ranging measurement is

$$
\begin{aligned}
\mathbf{C}_i &= \frac{\partial r_i}{\partial \delta\mathbf{x}} \\
&= \left[\tfrac{\mathbf{f}(\mathbf{x})^\top}{||\mathbf{f}(\mathbf{x})||_2}, \quad \mathbf{0}_{1x3}, \quad -(\tfrac{\mathbf{f}(\mathbf{x})}{||\mathbf{f}(\mathbf{x})||_2} \hat{\mathbf{R}}_b^n \mathbf{S}(\mathbf{p}_{bt}^b))^\top, \quad \mathbf{0}_{1x6}, \quad 1 \right]
\end{aligned}
\tag{19}
$$

In situations where GNSS measurements are used, the following measurement model is used:

$$
\begin{aligned}
\mathbf{p}_{\text{gnss}}^n &= \mathbf{p}_{nm_g}^n + \mathbf{w}_{\text{gnss}} \\
&= \mathbf{p}_{nb}^n + \mathbf{R}_b^n \mathbf{p}_{bm_g}^b + \mathbf{w}_{\text{gnss}} \\
&= \underbrace{(\hat{\mathbf{p}}_{nb}^n + \delta\mathbf{p})}_{\mathbf{p}_{nb}^n} + \underbrace{\hat{\mathbf{R}}_b^n(\mathbf{I}_3 + \mathbf{S}(\delta\mathbf{a}))}_{\mathbf{R}_b^n} \mathbf{p}_{bm_g}^b + \mathbf{w}_{\text{gnss}} \\
&= (\hat{\mathbf{p}}_{nb}^n + \delta\mathbf{p}) + \hat{\mathbf{R}}_b^n(\mathbf{I}_3 - \mathbf{S}(\mathbf{p}_{bm_g}^b))\delta\mathbf{a} + \mathbf{w}_{\text{gnss}}
\end{aligned}
\tag{20}
$$

where each receiver antenna has its own lever arm $\mathbf{p}_{bm_g}^b$. The Jacobian of (20) for one receiver is

$$
\mathbf{C}_i = \frac{\partial \mathbf{p}_{\text{gnss}}^n}{\partial \delta\mathbf{x}} = \left[\mathbf{I}_3, \quad \mathbf{0}_{3x3}, \quad -\hat{\mathbf{R}}_b^n \mathbf{S}(\mathbf{p}_{bm_{g,i}}^b), \quad \mathbf{0}_{3x7} \right] \tag{21}
$$

The Jacobians are evaluated using the current state estimates. Linearization of (17) is used to predict the covariance of the error states. Correction of the error states and the covariance is conducted when aiding measurements are received. Finally, the error states are reset to zero:

$$
\hat{\mathbf{x}} \leftarrow \hat{\mathbf{x}} \otimes \delta\mathbf{x} \tag{22}
$$

The reset step is more complicated for the attitude since the nominal state and error state have different number of elements. The following equation is used [11]:

$$
\begin{aligned}
\delta\mathbf{q}(\delta\mathbf{a}) &\leftarrow \frac{1}{16 + \mathbf{a}^\top \mathbf{a}} \begin{bmatrix} 16 - \delta\mathbf{a}^\top \delta\mathbf{a} \\ 8\delta\mathbf{a} \end{bmatrix} \\
\mathbf{q}_b^n &\leftarrow \mathbf{q}_b^n \otimes \delta\mathbf{q}(\mathbf{a})
\end{aligned}
\tag{23}
$$

where $\otimes$ is the quaternion product.

D. Practical Aspects

The models for the angular rate and acceleration biases were chosen as a Markov model. A pure random-walk model could also be chosen, particularly for missions of short duration. For longer missions, it is beneficial to keep the inertial bias from growing in an unbounded fashion and that is why the time constant matrices are included.

Another design choice is how the UWB ranging bias is modeled. In principle, each anchor has its own unique bias because they run on their own printed circuit board (PCB). However, the practical explanation for the bias is the processing time on the PCBs in the anchor and tag, and the hardware design of the PCB is similar for all anchors. Therefore, by assuming that clock drift is negligible in between sending and receiving a signal, a single common bias is a reasonable assumption. An alternative is to use an individual bias for each anchor. Both alternatives are investigated in Section VI-D.

Tuning of the filter is also a design choice and affects the accuracy. The process noise covariance $\mathbf{Q}$, defined in [11], is based on the IMU characteristics. This matrix is discretized using van Loan's method or another suitable discretization method [32]. The measurement noise covariance $\mathbf{R}$, also defined in [11], is based on the accuracy of the UWB ranging measurements and (when used) GNSS measurements.

V. Experimental Setup

The purpose of the experiments is to investigate if UWB ranging measurements is a suitable aiding principle for ferries during harbor maneuvering. This involves real-time estimation of all states using the MEKF, calibration of UWB anchor positions and real-time estimation of sensor bias.

A. Navigation suite

The following navigation suite was used to collect full scale experimental data:

- Adis 16490 MEMS IMU measuring specific force and angular rate at a frequency of $250\,\mathrm{Hz}$ with specifications given in [33].
- Two uBlox Neo M8T GNSS receivers measuring pseudoranges at a rate of $5\,\mathrm{Hz}$ [34] with two Harxon HX-GS288A antennas.
- UWB ranging system produced by beSpoon with one tag and five anchors. The system measures the range between the tag and anchors (if in line of sight and within measurement range) at a rate of $12\,\mathrm{Hz}$. The system is described more closely in [27].

The robotic operating system (ROS) was used to log experimental data for post processing.

B. Experiments

The passenger ferry displayed in Figure 1 was used as experimental platform to collect relevant data. The ferry operates between Trondheim and Vanvikan in Norway. The sensor suite was mounted on top deck and data was captured from eight different crossings from Vanvikan to Trondheim. The data was captured on two different days. Data from two crossings on each day will be presented in this paper to avoid repetitive analyses. The UWB anchors were mounted on the harbor in Trondheim as displayed in Figure 2. Three anchors were placed on the quay, and two of the anchors on the opposite side to improve the geometry of the localization problem. All anchors were placed at approximately the same height due to restrictions on the quay. Consequently, the vertical localization accuracy is degraded because of the resulting ill-conditioning. The anchors were removed and installed manually on both days. A small difference in the exact anchor position might therefore be present between the two days. In practice, a single calibration is sufficient.

The passenger ferry operated with the regular schedule without any adjustments to their normal operation. Consequently, the data represents the expected ferry motion during docking by a human operator. The docking area is shielded from the open sea so the wave influence can be neglected within the harbor in calm weather. The ferry moored on the left side hand of the quay where anchors 1-3 were placed. This can be seen in Figures 1 and 2. The weather conditions were calm and sunny during both days of data collection.

Fig. 1. Passenger ferry used to collect data on the docking location in Trondheim.

The origin of the body frame was placed in the center of the IMU. Lever arms from the IMU to the GNSS antennas and the UWB tag were measured manually in the body frame. Since the ferry position is in the origin of body, the measurements from GNSS were transformed to this location using the lever arms and the attitude of the ferry. Consequently, there is a coupling between the attitude estimator and the translational motion estimator. This also influences the reference since the position measurements from RTK GNSS were transformed to the body frame in the same manner. Therefore, the reference has a small uncertainty originating from the potential error in the estimated attitude (primarily heading since the roll and pitch angles were small).

The GNSS antennas were mounted on one side of the wheelhouse due to physical constraints. Thus, GNSS signals from parts of the hemisphere were blocked by the wheelhouse. This is considered to be realistic since parts of the hemisphere may be blocked in urban harbors.

C. Calibration of UWB anchor placement

A fundamental requirement for the UWB-aided localization system is accurate knowledge of the anchor positions. It is not possible to estimate the anchor positions in real-time using only the UWB ranging measurements. However,

Fig. 2. Docking area seen from above with UWB anchor placement. Courtesy of Google Earth.

it is possible to identify the anchor positions through a calibration procedure based on experimental data. A simpler alternative is to measure the position of each anchor manually with RTK GNSS using a survey antenna, but can be unreliable due to GNSS vulnerabilities.

The calibration procedure requires a calibration data set where the position of the tag is known, e.g, through RTK GNSS. The same issues with respect to reliability and accuracy for RTK GNSS persist but can be minimized by moving the tag further from buildings. Identifying the anchor positions is constructed as an optimization problem. Let r_{ij} be the range between anchor *i* and *j* (can be measured with range laser for example) and let r_{ti} be the range between the tag and anchor *i*. The optimization problem is formulated as

$$\begin{aligned} \min_{\mathbf{X}} \quad & \sum_{t=1}^{T}\sum_{i=1}^{N} s_{ti}^2 + w\sum_{i=1}^{N}\sum_{j=1}^{N}\sigma_{ij}^2 \\ s.t. \quad & (\mathbf{e}_i-\mathbf{e}_j)^\top \boldsymbol{Y}(\mathbf{e}_i-\mathbf{e}_j)+\sigma_{ij}=r_{ij}^2, \forall(i,j)\in N_a \\ & \begin{bmatrix}\mathbf{p_t}\\ \mathbf{e}_i\end{bmatrix}^\top \begin{bmatrix}\mathbf{I}_3 & \mathbf{X}\\ \mathbf{X}^\top & \mathbf{Y}\end{bmatrix} \begin{bmatrix}\mathbf{p_t}\\ \mathbf{e}_i\end{bmatrix} + s_{ti} = r_{ti}^2, \forall(t,i)\in N_s \\ & \mathbf{Y}=\mathbf{X}^\top\mathbf{X} \end{aligned} \tag{24}$$

where s_{ti} and σ_{ij} are slack variables introduced to handle measurement noise in the RTK GNSS and UWB ranging measurements and noise in the internal distance between anchors, respectively. T and N are the number of time steps and anchors, respectively. N_a and N_s are the index set of available range measurements and index set of in-between anchor measurements, respectively. $\mathbf{p}_t$ is the RTK-GNSS position of the tag, $\mathbf{e}_i$ is a unit vector where element i is one, and $\mathbf{X}$ is an unknown matrix with the position of all anchors where each anchor has its own row. w is a scalar weight that is used to weight the internal distance between the anchors and the measurements between the tag and anchors.

UWB measurement bias is not included in (24). However, the bias can be identified as part of the calibration procedure if it is assumed that a single common (constant) bias is present for all anchors as mentioned in Section IV-D. The optimization problem can be solved several times for different values of the bias. The bias is included by subtracting the chosen bias from each ranging measurement r_{ti}. The best estimate of the bias is the value that minimizes the re-projection error when all bias values are compared. This is computationally expensive but can be calculated once as part of a calibration procedure. The bias is caused by processing time and is therefore positive. Values from zero to the maximum expected bias should therefore be used with a suitable step in between. An example would be to solve the optimization problem for bias values of $0\,\mathrm{cm}$, $5\,\mathrm{cm}$, $10\,\mathrm{cm}$ and up to a chosen maximum value.

Equation (24) can be solved by a nonlinear program (NLP) or as a semi-definite problem (SDP) if the equality $\mathbf{Y} = \mathbf{X}^\top\mathbf{X}$ is relaxed to an inequality constraint $\mathbf{Y} \geq \mathbf{X}^\top\mathbf{X}$. The relaxation reduces the computational footprint at the cost of a less accurate solution in general. Both a NLP and the SDP are used experimentally in Section VI-C. The NLP is initialized using the GNSS-measured anchor positions to ensure that the starting point is close to the correct global minimum. Moreover, additional constraints such as relative height difference can be added if more information about the installment is available. This will help the solver in finding a feasible solution.

VI. EXPERIMENTAL RESULTS

This section contains several case studies. The goal is to close the gap between the theoretical use of such a system and the practical performance in a relevant environment, namely navigation for a passenger ferry during harbor maneuvering. Four different case studies are carried out to validate the use of UWB experimentally.

A. INS Tuning

The data sheet of the IMU [33] was used for initial tuning of the filter. The IMU was strapped to the floor of the ferry and was affected by vibrations from the hull and the engines. Consequently, the measured noise levels were significantly higher than what the data sheet indicates. Therefore, the mean standard deviation of the measurements in one data set was used to estimate the noise level of the IMU and used to tune the ESKF. The noise level of the bias model was tuned with the values in the data sheet and then scaled down by a factor of ten to avoid rapid changes in the estimated bias. This is motivated by the fact that it is difficult to estimate the accelerometer bias when the attitude is estimated simultaneously without specific maneuvers due to lack of observability (the ship moved along an approximately straight-line during docking).

The noise in the UWB measurements was tuned with a standard deviation of $10\,\mathrm{cm}$ which is in line with the observed accuracy of the system. The noise level of the RTK-GNSS measurements was tuned with a standard deviation of $10\,\mathrm{cm}$ in the horizontal plane and $50\,\mathrm{cm}$ in the altitude assuming a floating-point solution (not fixed).

The states were estimated at a frequency of $31.25\,\mathrm{Hz}$ which means that the IMU measurements were sub-sampled with a factor of eight from the original frequency.

B. Case 1 - INS aided by UWB

The first case studies the general performance of the INS aided by UWB for localization in a harbor area. The solution is compared with an INS aided by a dual-antenna RTK GNSS, which is considered to be state of the art for localization without a gyrocompass. Data from four different dockings have been analyzed. A constant pre-calibrated value for the UWB bias was used in this case. The bias was identified as the value that provided the minimum re-projection error for anchor positions using the optimization problem presented in Section V-C. This procedure is compared with real-time estimation of the UWB bias in Section VI-D. The constant bias value was identified to be $85\,\mathrm{cm}$. A virtual altitude measurement was added to aid the filter in the vertical direction since it is known that the ferry operated on the sea surface. The effect of this is studied in Section VI-E. Without the virtual measurement, the vertical dilution of precision (DOP) in the UWB measurements induces errors into the horizontal plane.

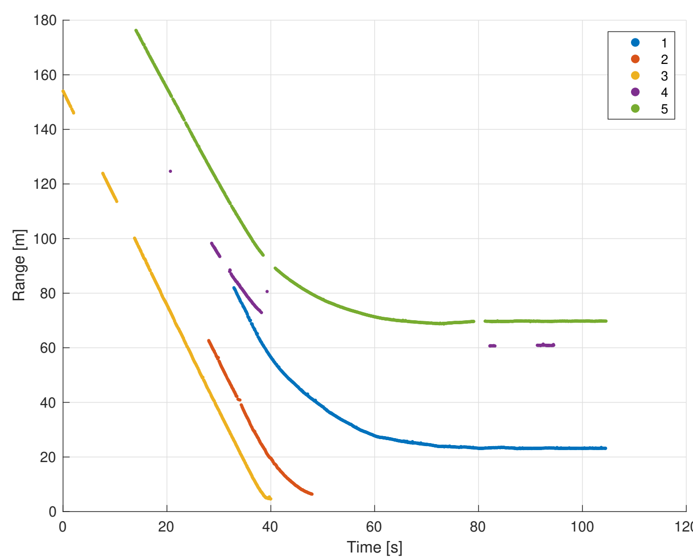

Fig. 3. Measured range between tag and anchors in the first dataset

Figures 3 and 4 show two examples of range measurements received during the approach to Trondheim in two datasets. Figure 3 shows a situation where one anchor was unreliable (number 4) and not many range measurements were available at the same times. This figure supports the choice of tight integration and exemplifies the drawback with multilateration and loose coupling. The maximum measured range of the system was approximately $175\,\mathrm{m}$. Anchors two and three were only able to provide range measurements in the beginning since the ferry moved passed the location of these anchors during the docking maneuver. The maximum measured range for the second dataset (Figure 4) was about 270 meters, and more range measurements were available in this experiment. Sensitivity to the elevation between anchor and tag antennas, and varying line of sight conditions during the maneuver are the two main factors for the varying ability to receive range measurements. The elevation between the antennas is also affected by tides, which changes the altitude of the ferry as much as two meters within a few hours.

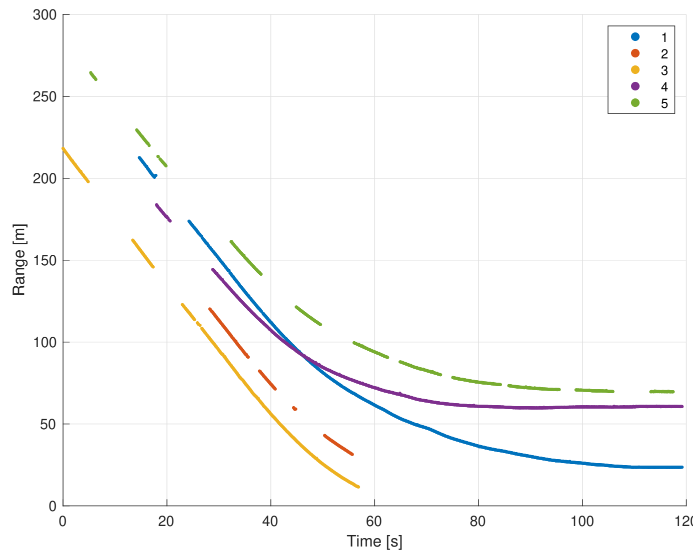

Fig. 4. Measured range between tag and anchor in the second dataset

Figures 5 and 6 show the estimation error in position from the same datasets when the INS aided by UWB is compared with the INS aided by two RTK-GNSS receivers. The dotted lines illustrate the estimated two times standard deviation of the estimation error. Note that the RTK measurements were used to initialize the UWB aided system before the RTK measurements were removed after about $15\,\mathrm{s}$ in the first data set ($25\,\mathrm{s}$ in second data set). Both figures show that the position error increases after the switch to UWB, but that the estimated error decreases somewhat when the ferry approaches the dock. The position error is within $30\,\mathrm{cm}$ for most of the docking period. Figures 3 and 4 also show that the number of measurements was smaller initially than later in the estimation period. This is also reflected by the estimated standard deviation which decreases with enough ranging measurements. The standard deviation also shows that the estimated position is within the confidence bounds, and that the covariance estimate is conservative (large margin to bounds). Consequently, the adjustable noise terms from the IMU measurements and the UWB ranging measurements could have been reduced to narrow the margin of the confidence bounds.

Figure 7 shows the attitude error in the first dataset. The attitude error is similar in magnitude for the second dataset. The roll and pitch errors are within $0.2°$ which makes sense since the same IMU was used for both the reference and the UWB-aided localization system. Note that the estimated standard deviation in yaw increases with time since a single UWB tag was used to estimate the heading. Such a solution is not observable without an additional tag or another heading reference onboard the ship. Nevertheless, the results show that the yaw angle can be predicted accurately for the necessary period near the dock without significant increase in the covariance or drift in the estimates.

Average performance statistics are presented in Tables I to III. Metrics from a third dataset are included for

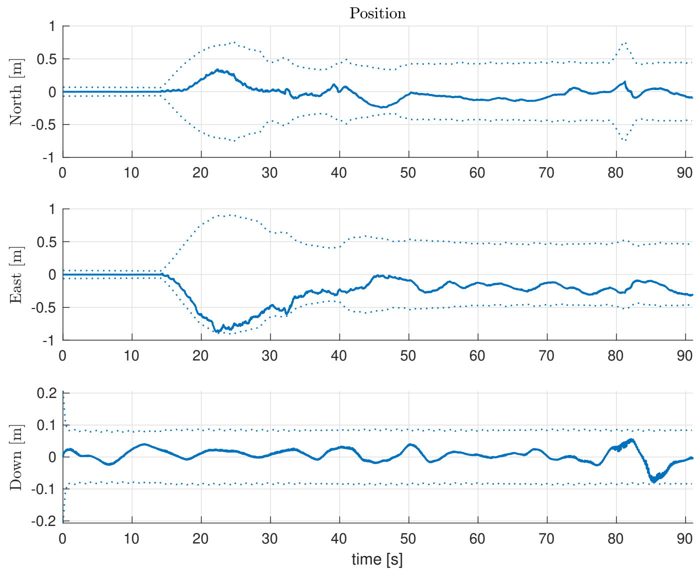

Fig. 5. Estimation error in position in the first dataset

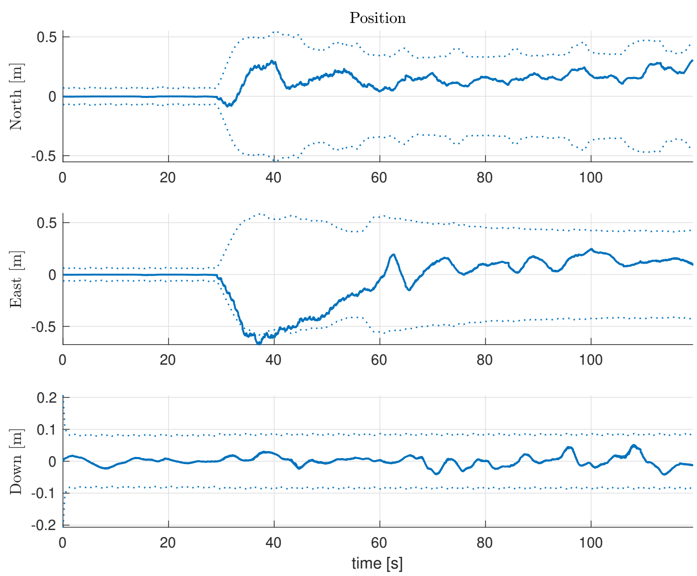

Fig. 6. Estimation error in position in the second dataset

completeness. Figure 8 shows an interesting situation where the estimation error in the horizontal plane is much larger initially. This is from a fourth dataset where ranging measurements from anchors four and five were missing initially. Therefore, only ranging measurements from one side of the quay (right side of Figure 2) were available. Moreover, the other anchors were located along the same line of sight during the approach. The ferry approach was from the direction of the bottom left corner in Figure 2. Consequently, the estimation of the horizontal position is not observable and a dead reckoning situation occurs. This is also reflected in the estimated standard deviation which increases to several meters, both in north and east positions. Ranging measurements from both sides of the

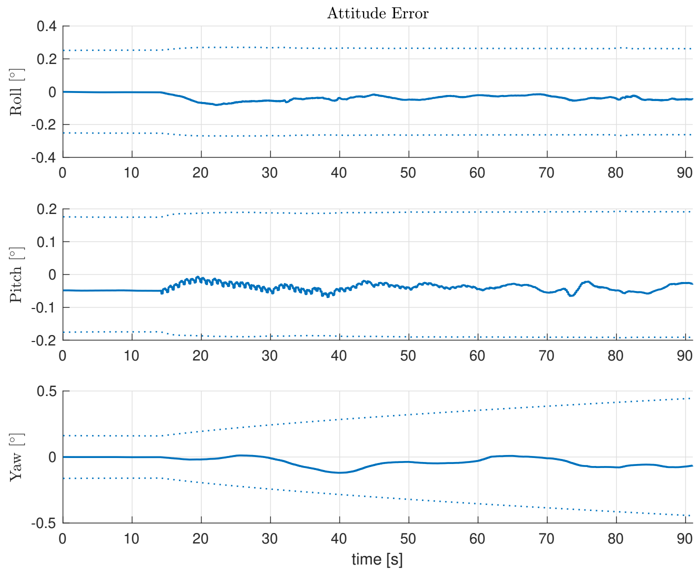

Fig. 7. Estimation error in attitude in the first dataset

quay became available after about 25 seconds and the filter quickly converges towards the reference afterwards. Moreover, the same is observed for the estimated standard deviation. The horizontal position error is below $20\,\mathrm{cm}$ in the end. Since the estimation error is within the bounds of the standard deviation, the estimates are consistent and the navigation system is still reliable even though the accuracy is significantly degraded. The attitude error is similar for this dataset so the increase in position error is not influencing the attitude error notably which is explained by the dead reckoning using the ARS and aiding in roll and pitch from the accelerometers.

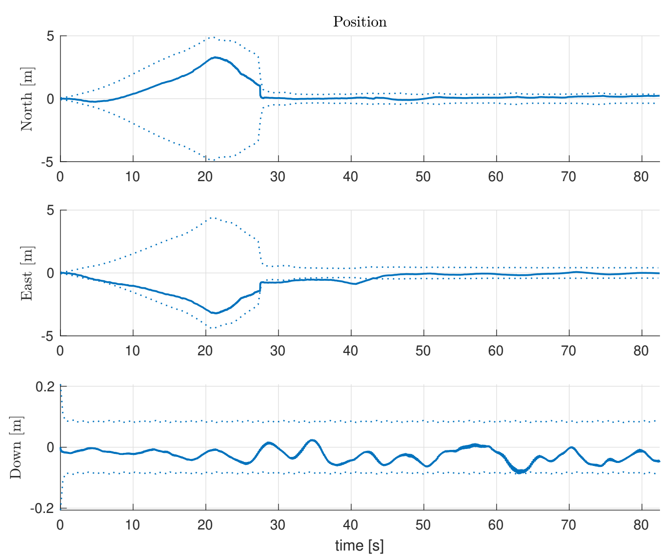

Fig. 8. Estimation error in position in the fourth dataset

TABLE I
PERFORMANCE METRICS OF THE FIRST DATASET

	north [m]	east [m]	down [m]	norm [m]
ME:	-0.01	-0.28	0.00	0.28
STD:	0.11	0.21	0.02	0.24
RMSE:	0.11	0.34	0.02	0.36

TABLE II
PERFORMANCE METRICS OF THE SECOND DATASET

	north [m]	east [m]	down [m]	norm [m]
ME:	0.15	-0.06	0.00	0.16
STD:	0.07	0.25	0.02	0.26
RMSE:	0.17	0.26	0.02	0.31

Figure 9 shows the position error during a pure dead reckoning situation using the INS. Position aiding measurements were removed in the intervals $425\,\mathrm{s}$ to $475\,\mathrm{s}$ and $625\,\mathrm{s}$ to $675\,\mathrm{s}$ and the horizontal position error grows to $32\,\mathrm{m}$. The rate at which the error grows is comparable to Figure 8. Therefore, ranging measurements from the same line of sight are not sufficient to avoid dead reckoning in the horizontal position. The difference in performance in the vertical position originates from the virtual altitude measurements used in the filter in Figure 8. Note that the tuning of the dead reckoning system could likely be improved so the rate at which the error grows does not represent the best possible dead reckoning performance. Nevertheless, the results show that ranging measurement along the same line is not sufficient to avoid drift in the horizontal position, but that the estimation error is within the estimated confidence bounds.

The results have intentionally been presented as a function of time. It is also interesting to consider how the ranging distance affects the accuracy. The system was tested on land and the measurement error in the UWB ranging system was not affected notably by the ranging distance. The same was also observed for the UWB bias, which remained constant across different ranges. This is reasonable since the bias is assumed to be from the processing time in the anchor and tag. However, increasing the ranging distance increases the probability of measurement dropout due to reduction in the signal strength. Loosing measurements from one or more anchors will obviously reduce the accuracy of the estimates in periods with few measurements. Observability issues will arise if less than three anchors are reachable. Consequently, the distance in between the tag and anchors is important for the estimation accuracy due to measurement dropout. Measurement dropout is typically most problematic in the initial phase since the range between the ferry and anchors is decreasing with time when the ferry moves closer to the quay. Drift and reduced accuracy should be expected initially if few ranging measurements are available since the estimates will be based on dead reckoning without sufficient correction. Careful anchor placement and increasing the number of anchors are viable strategies that can mitigate measurement dropout.

TABLE III
PERFORMANCE METRICS OF THE THIRD DATASET

	north [m]	east [m]	down [m]	norm [m]
ME:	-0.28	-0.56	0.00	0.63
STD:	0.10	0.20	0.02	0.22
RMSE:	0.30	0.60	0.02	0.67

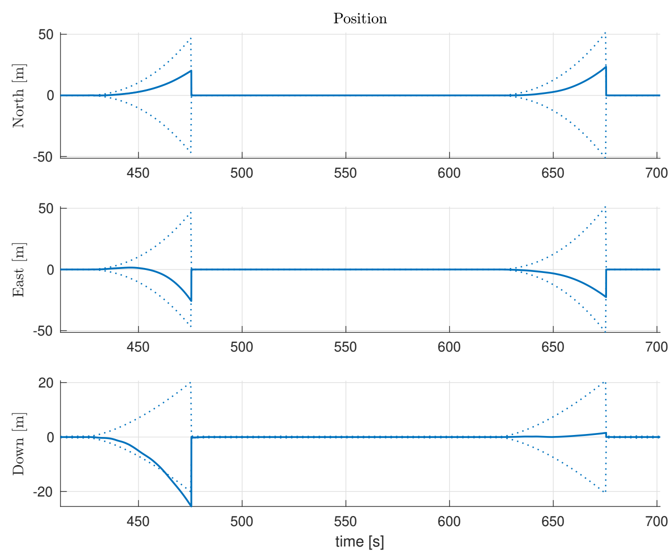

Fig. 9. Estimation error in position during dead reckoning (pure INS without aiding)

C. Case 2 - Anchor Position Calibration

This case investigates how accurate the position of the UWB anchors can be calibrated. This is key for the accuracy of the localization system. The calibration procedure in Section V-C is used to investigate how the location of the anchors can be obtained. The results presented in this section are based on three simulations. Simulations are necessary to investigate the validity of the method since the exact placement of the anchors in the field are unknown.

The first simulation is based on the trajectory of the ship and evaluates how precisely the position of the anchors can be obtained with RTK GNSS and the UWB ranging measurements from experimental data. The second simulation is based on an elliptical calibration path that makes sense from a theoretical perspective and can be conducted with the ferry. An elliptical path is beneficial since measurements are available from all angles between the tag and anchors. This will cancel systematic bias originating from the mounting or from structures blocking the range measurements. The third simulation is based on the same elliptical path in the horizontal plane, but also includes a variation in altitude increasing from the sea surface to eight meters above the sea surface making it a spiral. Such a trajectory can be followed using a drone. The calibration paths in the horizontal plane are shown in Figure 10 along with the anchor placements. The spiral path is not shown in the figure, but has the exact same trajectory in the horizontal plane as the elliptical path. Figure 10 also visualizes that the ferry moored close to three of the anchors as the blue line illustrates. The blue line is the typical trajectory of the ferry when moving towards the quay and the ferry approaches from the bottom left corner.

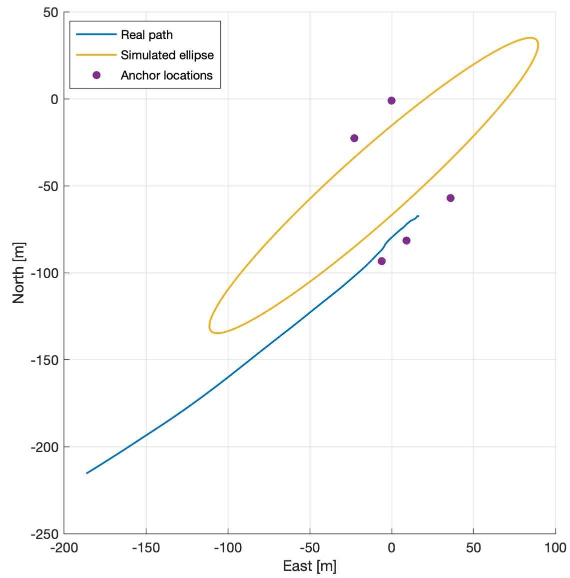

Fig. 10. Calibration paths in the horizontal plane.

UWB measurements were simulated by using the true position of the ship to calculate the range between the ship and the anchors. A range bias of $90\,\mathrm{cm}$ was added to the simulated UWB measurements. Moreover, white Gaussian noise with a standard deviation of $10\,\mathrm{cm}$ was added to the measurements. This is in line with the typical docking behavior of UWB systems, as described in Section V-A.

Both the NLP solution and relaxed (SDP) solution were solved in Matlab using the method described in Section V-C. The optimization was performed for different values of the bias to find the bias that minimizes the re-projection error of the anchor positions. Consequently, the bias was also be identified through the calibration procedure under the assumption of being constant. Moreover, relative height differences in between the anchors were added as constraints since the paths lack altitude variations. This guides the optimization algorithm to the correct solution. These relative height differences can be identified experimentally by measuring the vertical distance between each anchor and the sea surface. A range laser was used to find these constraints in the experimental data.

The first simulation was based on a simulation of the typical docking path of the ship. It is illustrated as the blue line in Figure 10 and has a constant height due to the sea surface (tide variations for the duration of the calibration are neglected). The results are summarized in Table IV. Only the exact method with relative z constraints was able to find the correct bias and has the smallest root mean squared error (RMSE) for the anchor positions. However, the exact method without relative z constraints was struggling to find the vertical positions of the anchors as seen by the total error in Table IV. Note that the accuracy will increase with the number of available ranging measurements and these results are based on the experimental trajectory of the ship in one dataset, and the times when UWB ranging measurements were available.

TABLE IV
PERFORMANCE STATISTICS FOR ANCHOR CALIBRATION USING THE SHIP DOCKING PATH.

Algorithm	Constraints	Horizontal RMSE [m]	Total RMSE [m]	Chosen bias [m]
SDP	None	0.52	2.34	1.00
SDP	Relative z	0.53	0.58	1.00
Exact	None	0.18	14.65	0.95
Exact	Relative z	0.19	0.33	0.90

The second simulation was based on the elliptical path marked in yellow in Figure 10. This is a suggested calibration path that theoretically improves the horizontal dilution of precision. The exact optimization method and the SDP relaxation identified the correct bias, both with and without relative height constraints. The RMSE of the calculated anchor positions are much smaller with this trajectory but also needs the z constraints to find the correct vertical position. This is supported by the total error in Table V. The elliptical path is therefore a better calibration trajectory than the typical ship trajectory. This is expected and shows that a tailor-made calibration maneuver should be conducted to find the anchor locations in practice.

TABLE V
PERFORMANCE STATISTICS FOR ANCHOR CALIBRATION USING THE ELLIPTICAL PATH.

Algorithm	Constraints	Horizontal RMSE [m]	Total RMSE [m]	Chosen bias [m]
SDP	None	0.03	8.47	0.90
SDP	Relative z	0.03	0.08	0.90
Exact	None	0.02	16.92	0.90
Exact	Relative z	0.01	0.05	0.90

Table VI shows the same metrics for the spiral path with altitude variations. The most significant difference compared to the elliptical path is that the need for relative z (altitude) constraints is avoided when the spiral path is used. The accuracy is improved with relative z constraints, but not in the same extent as for the other paths. The results show that an elliptical path is sufficient if relative z constraints are known and that a spiral path is necessary if these constraints are unknown.

Figure 11 shows the re-projection error of all methods as a function of the UWB bias when using the ship docking path for calibration. The most appropriate bias is identified as the value that minimizes this curve. It is apparent that it is difficult to find a feasible solution without z constraints. Especially the total error (including the re-projection error in the vertical plane) has several minima without the additional constraint and it is hard to find a feasible solution for the NLP. The re-projection error using the elliptical path is displayed in Figure 12 and shows

TABLE VI

PERFORMANCE STATISTICS FOR ANCHOR CALIBRATION USING THE SPIRAL PATH.

Algorithm	Constraints	Horizontal RMSE [m]	Total RMSE [m]	Chosen bias [m]
SDP	None	0.04	0.37	0.90
SDP	Relative z	0.03	0.12	0.90
Exact	None	0.02	0.38	0.90
Exact	Relative z	0.01	0.19	0.90

that the re-projection curve has the minimum value at the correct bias. The bias was identified to be $85\,\mathrm{cm}$ for the experimental data.

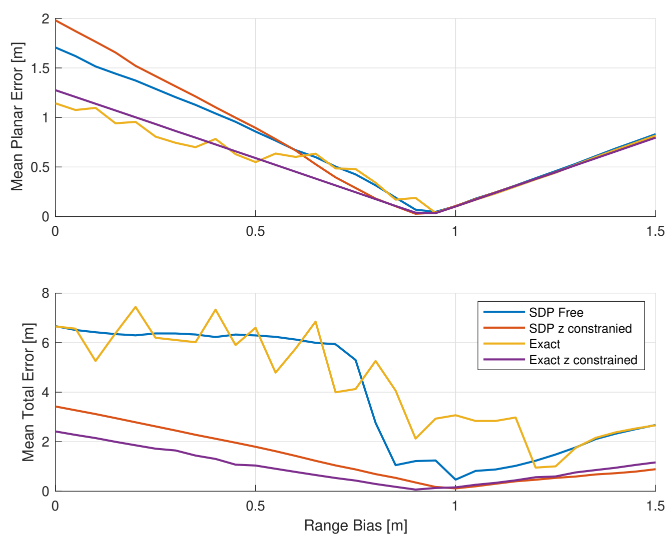

Fig. 11. Re-projection error using the ship docking path

For the field experimental data, the exact method with relative z constraints was used to find the anchor positions. The accuracy of the anchor positions are expected to be in line with the values in Table IV. Moreover, RTK GNSS with a survey antenna was used to verify the integrity of the calibration results.

D. Case 3 - UWB Bias Estimation

This case studies estimation of UWB ranging bias. Two alternatives are available. The first alternative is to use the constant value identified in the previous section. This is a static calibration that can be conducted once as part of a calibration procedure, but assumes that the bias remains constant (and time independent) for all anchors. This assumption makes sense from a practical viewpoint when the UWB ranging bias originates from processing time in the UWB tag and anchor firmware.

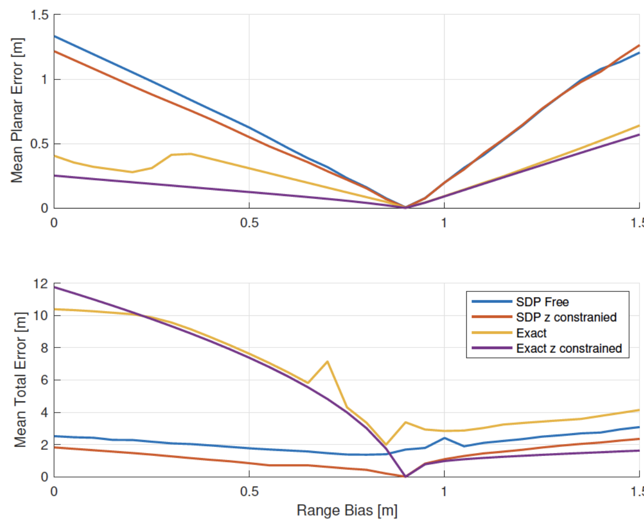

Fig. 12. Re-projection error using elliptical path

The second alternative is to estimate the UWB ranging bias online as part of the localization algorithm as described in Section IV. This is beneficial if the anchor calibration is uncertain, or the bias varies. It is also possible to include one bias for each anchor using this strategy, but observability is challenging without additional GNSS measurements. Real-time estimation of the bias is compared experimentally with a pre-calibrated bias value in this section. The results are based on the same datasets as in Section VI-B. Note that the results in Section VI-B used the pre-calibrated value of the UWB ranging bias ($85\,\mathrm{cm}$).

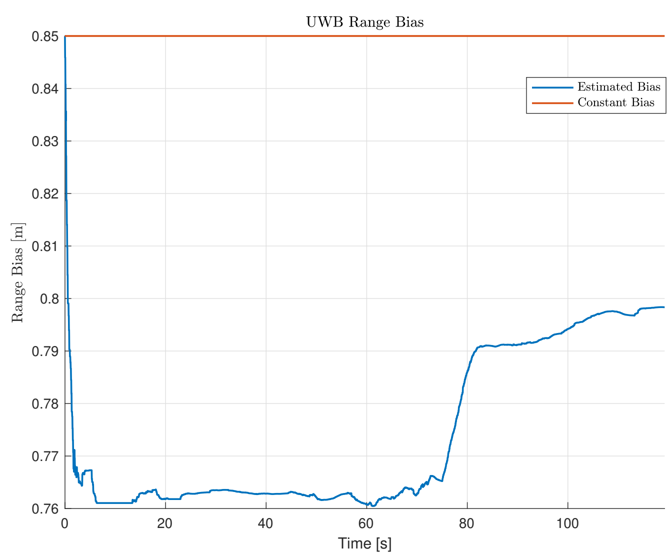

Fig. 13. Online estimated UWB bias vs pre-calibrated bias

Figure 13 shows the estimated UWB ranging bias when a single common bias was assumed for all anchors in the second dataset. The switch from RTK-GNSS measurements to UWB ranging measurements occurred at about 30 seconds. The estimated UWB bias was initialized at the constant pre-calibrated value of $0.85\,\mathrm{m}$. The estimated bias converges towards a value of $0.70\,\mathrm{m}$ near the end. Figure 14 shows the estimation error in position for the second dataset with online bias estimation and with the pre-calibrated value. Figure 15 shows the estimation error in attitude for the same dataset. A similar behavior is observed for both filters. A small difference is observed in pitch after 30 seconds during the switch from RTK to UWB.

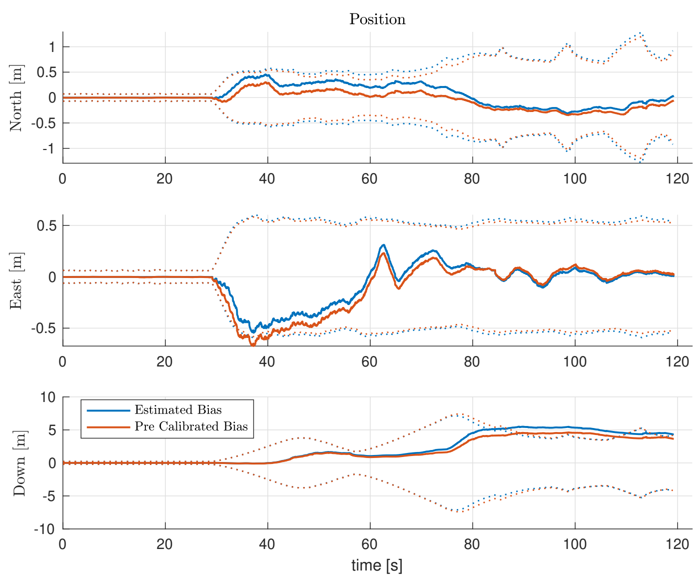

Fig. 14. Estimation error in position with UWB bias estimation

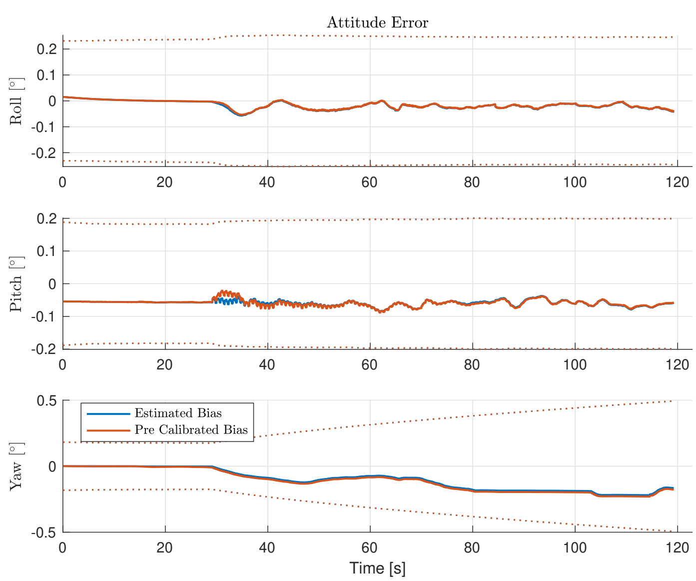

Fig. 15. Estimation error in attitude with UWB bias estimation

The performance of the filter with real-time bias estimation is summarized for all datasets in Tables VII to IX. These values can be compared with the values in Table I to Table III which show the performance when using the pre-calibrated bias value. The performance is comparable for both strategies, and the best strategy varies between the datasets. A clear trend is not observed. However, it is obvious that the UWB ranging bias is significant and should be identified before the system is used, and/or estimated online.

TABLE VII
PERFORMANCE METRICS OF FIRST DATASET WITH REAL-TIME BIAS ESTIMATION

	north [m]	east [m]	down [m]	norm [m]
ME:	0.09	-0.21	0.00	0.23
STD:	0.11	0.20	0.02	0.23
RMSE:	0.15	0.29	0.02	0.33

TABLE VIII
PERFORMANCE METRICS OF SECOND DATASET WITH REAL-TIME BIAS ESTIMATION

	north [m]	east [m]	down [m]	norm [m]
ME:	0.33	0.01	0.00	0.33
STD:	0.09	0.23	0.02	0.25
RMS:	0.34	0.23	0.02	0.41

TABLE IX
PERFORMANCE METRICS OF THIRD DATASET WITH REAL-TIME BIAS ESTIMATION

	north [m]	east [m]	down [m]	norm [m]
ME:	-0.07	-0.44	0.00	0.44
STD:	0.09	0.18	0.02	0.21
RMSE:	0.12	0.48	0.02	0.49

It has been assumed that a single common bias can be used for all anchors so far. An independent bias can be estimated for each anchor and this strategy will be investigated for completeness. The first and second dataset will be used. Using independent anchor biases can account for differences in between the anchors, which may occur even though the hardware design is identical. In addition, estimating one bias for each anchor can potentially compensate for other errors such as uncertainty in the anchor locations. Figures 16 and 17 show the position error in the horizontal plane when using a pre-calibrated bias, a single real-time estimated bias and multiple real-time estimated biases (one for each anchor). A significant difference is not observed in any dataset. However, smaller differences are present and can be important in shorter time periods. Nevertheless, a clear benefit of using individual biases for each anchor has not been identified in this research.

The results in this section have shown that a single pre-calibrated bias is sufficient to maintain the desired performance. Consequently, this is perhaps the most attractive approach for this UWB ranging technology since computation time and complexity can be reduced by removing UWB bias from the real-time estimation problem. This is also supported by the fact that the clock frequency in the anchors is expected to be constant over time, which imply that the bias is constant. However, it might be necessary to include bias in the estimation problem for other UWB ranging systems, and this has been proven to be a viable strategy in this section.

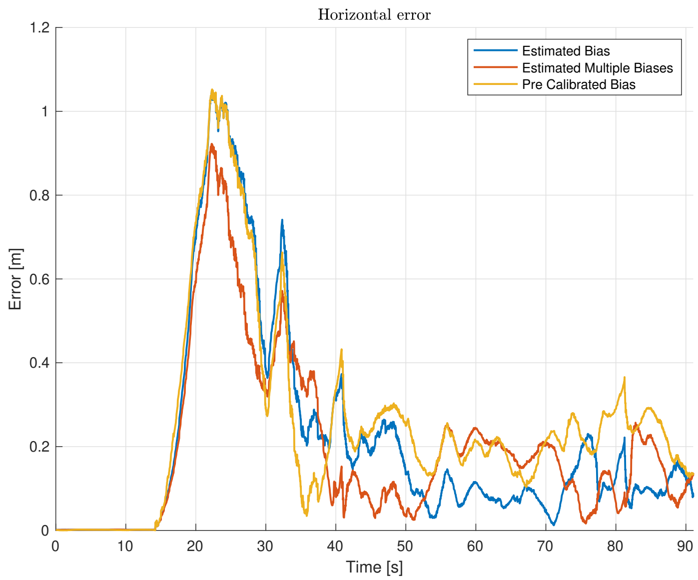

Fig. 16. Error in horizontal position with UWB bias estimation in dataset 1

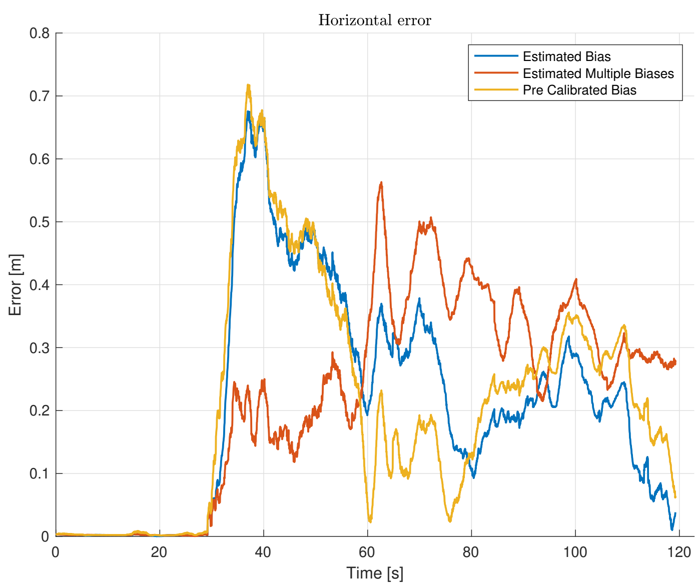

Fig. 17. Error in horizontal position with UWB bias estimation in dataset 2

E. Case 4 - Virtual Altitude Measurement

The final experimental study of this paper concerns the virtual altitude measurement mentioned in Section VI-B. Surface vessels operate on the sea surface and the altitude is constant as long as the docking operation takes place in a short time period with calm weather conditions (neglecting wave and tide influence). Consequently, a virtual altitude measurement can be included to aid the estimator since the geometry of the UWB anchors restricts the observability along the vertical axis (vertical dilution of precision). The virtual measurement is added to keep the altitude at a reasonable level. If the altitude error becomes too large, it can both influence the estimated UWB ranging bias, the horizontal position, and the heading of the vessel. This section compares the UWB-aided INS with and without virtual altitude measurements. The reference is still the RTK-aided INS. In practice, tide models can be used to generate virtual measurements that compensate for tide variations. This is important if anchors are installed on structures not moving with the tides.

The altitude measurements were generated by utilizing the lever arm between the origin of the body frame and the altitude of the sea surface, which is assumed known in NED through RTK GNSS or a tide model. Thus, the difference between the origin of body and the sea surface must be known. The altitude of the sea surface is not constant in NED in larger areas due to the inherent flat-earth assumption and the curvature of the Earth. Nevertheless, the altitude is constant in a small local area, such as harbors, when tides and waves are neglected, or when shorter periods are considered. Virtual altitude measurements were assumed available at a rate of $10\,\mathrm{Hz}$ and with a standard deviation of $10\,\mathrm{cm}$. The attitude estimates were not affected by the virtual altitude measurement, so the analysis of attitude is neglected in this section. Only the second dataset is presented to keep the analysis brief, but the results were verified across the rest of the data.

Figure 18 shows the estimation error in position for four versions of the ESKF. Two filters used the real-time estimated bias (single common bias for all anchors) and two filters used the pre-calibrated value. Moreover, two filters used the virtual altitude measurement and two did not use the virtual altitude measurement. Note the range difference for the estimation error along the different axes. The estimation error along the vertical axis is much larger for the filters without virtual altitude measurements as seen in Figure 18. This is expected due to the vertical DOP for the UWB anchors. The horizontal accuracy is not affected significantly by the virtual altitude measurements.

Figure 19 shows the UWB ranging bias for the four filters. The real-time estimated UWB bias is different with and without the virtual altitude measurement. Thus, the bias is affected by the accuracy of the down position. This is interesting and shows the tight coupling between the states in the ESKF. Note also that the bias is equal initially when RTK-GNSS measurements were available. The difference appears when only UWB ranging measurements are used. This makes sense since the bias is observable with RTK-GNSS measurements, but observability issues arise without RTK-GNSS measurements. Therefore, it could be beneficial to freeze the bias or use the pre-calibrated value when GNSS measurements are unavailable in practical applications.

VII. Conclusions

The results presented in this research have shown that an inertial navigation system aided by UWB ranging measurements can replace RTK-GNSS measurements for ships in harbor maneuvering and docking. It was assumed

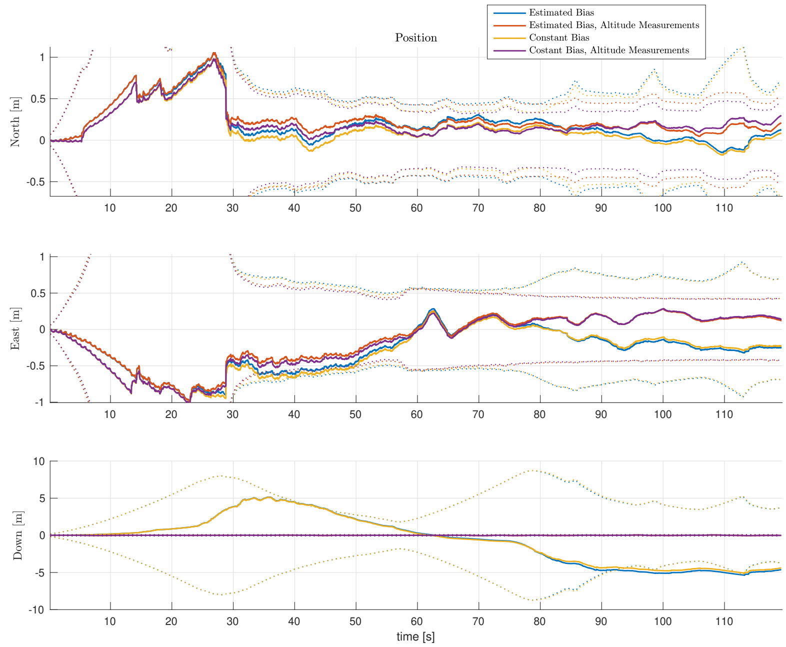

Fig. 18. Estimation error in position with virtual altitude measurement in dataset 2

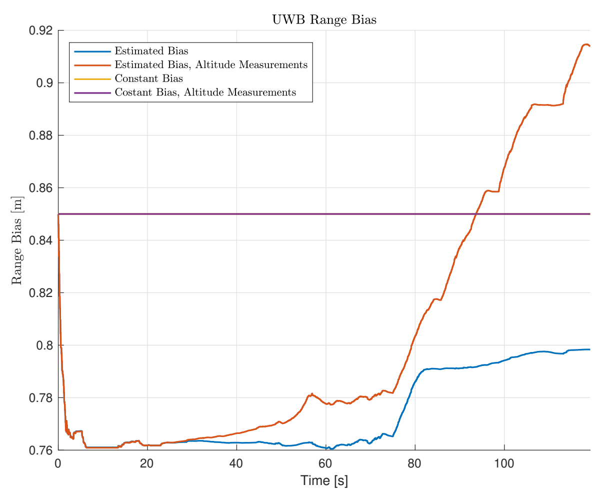

Fig. 19. Estimated UWB bias with virtual altitude measurement in dataset 2

that the localization system can be initialized properly before entering the harbor area. This includes having estimates of inertial sensor bias (IMU), and accurate estimates of position and attitude initially. The initialization was provided by an INS aided by RTK GNSS. The findings have been validated with a comprehensive amount of experimental data. The error in horizontal position was within $30\,\mathrm{cm}$ of the dual antenna RTK-aided reference, considered to be state of the art within ship localization without a gyrocompass. Moreover, the heading error was kept within $0.5\,\mathrm{deg}$.

It has also been shown that the range bias in the UWB measurements can be handled, both through calibration before the mission or through real-time estimation. One of the presented datasets had a significantly higher initial estimation error than the rest of the datasets. This was caused by a lack of UWB ranging measurements from one side of the harbor initially leading to a poor precision. If a UWB-aided INS is used in safety-critical applications, it is important to have enough anchors spread around in the operating area to ensure redundancy in case of hardware failure or loss of line of sight between the anchor and tag.

ACKNOWLEDGMENT & FUNDING

This work was supported by Kongsberg Maritime through the University Technology Centre (UTC) at NTNU. It was also in part supported by the Research Council of Norway through the Centres of Excellence funding scheme, project number 223254. The authors are grateful for the cooperation with Kongsberg Maritime and the feedback received from them during this work, in particular, Dr. Sverre Torben. We are also grateful for the cooperation with FosenNamsos that has given us access to acquire data on their vessel. The authors would like to thank associate professor Torleiv H. Bryne for access to his navigation framework in Matlab. Finally, we would like to thank Robert Rogne and Anders Pedersen for their significant contributions in the sensor payload.

REFERENCES

[1] A. Stateczny, C. Specht, M. Specht, D. Brčić, A. Jugović, S. Widźgowski, M. Wiśniewska, and O. Lewicka, "Study on the positioning accuracy of gnss/ins systems supported by dgps and rtk receivers for hydrographic surveys," *MDPI Energies*, vol. 14, no. 21, 2021.

[2] M. Specht, C. Specht, P. Dabrowski, K. Czaplewski, L. Smolarek, and O. Lewicka, "Road tests of the positioning accuracy of ins/gnss systems based on mems technology for navigating railway vehicles," *MDPI Energies*, vol. 13, no. 17, 2020.

[3] D. A. Divis, "GPS spoofing experiment knocks ship off course," *Inside GNSS News*, July 2013.

[4] D. Schmidt, K. Radke, S. Camtepe, E. Foo, and M. Ren, "A survey and analysis of the gnss spoofing threat and countermeasures," *ACM Comput. Surv.*, vol. 48, no. 4, 2016.

[5] J. Bhatti and T. E. Humphreys, "Hostile control of ships via false gps signals: Demonstration and detection," *NAVIGATION, Journal of the Institute of Navigation*, vol. 64, no. 1, pp. 51–66, 2017.

[6] X. Li, M. Ge, X. Dai, X. Ren, M. Fritsche, J. Wickert, and H. Schuh, "Accuracy and reliability of multi-gnss real-time precise positioning: Gps, glonass, beidou, and galileo," *Journal of Geodesy*, vol. 89, no. 6, pp. 607–635, 2015.

[7] P. D. Groves and Z. Jiang, "Height aiding, c/n0 weighting and consistency checking for gnss nlos and multipath mitigation in urban areas," *Journal of Navigation*, vol. 66, no. 5, p. 653–669, 2013.

[8] L. Yang, Y. Li, Y. Wu, and C. Rizos, "An enhanced mems-ins/gnss integrated system with fault detection and exclusion capability for land vehicle navigation in urban areas," *Gps Solutions*, vol. 18, no. 4, pp. 593–603, 2014.

[9] O. J. Woodman, "An introduction to inertial navigation," University of Cambridge, Computer Laboratory, Tech. Rep. UCAM-CL-TR-696, Aug. 2007. [Online]. Available: https://www.cl.cam.ac.uk/techreports/UCAM-CL-TR-696.pdf

[10] R. H. Rogne, T. H. Bryne, T. I. Fossen, and T. A. Johansen, "On the usage of low-cost mems sensors, strapdown inertial navigation, and nonlinear estimation techniques in dynamic positioning," *IEEE Journal of Oceanic Engineering*, 2020.

[11] T. Fossen, *Handbook of Marine Craft Hydrodynamics and Motion Control, Second Edition*. John Wiley & Sons, 2021.

[12] T. Taketomi, H. Uchiyama, and S. Ikeda, "Visual slam algorithms: a survey from 2010 to 2016," *IPSJ Transactions on Computer Vision and Applications*, vol. 9, no. 1, pp. 1–11, 2017.

[13] S. Wang, Y. Zhang, and F. Zhu, "Monocular visual slam algorithm for autonomous vessel sailing in harbor area," in *Saint Petersburg International Conference on Integrated Navigation Systems (ICINS)*, 2018.

[14] K. N. Lwin, N. Mukada, M. Myint, D. Yamada, A. Yanou, T. Matsuno, K. Saitou, W. Godou, T. Sakamoto, and M. Minami, "Visual docking against bubble noise with 3-d perception using dual-eye cameras," *IEEE Journal of Oceanic Engineering*, vol. 45, no. 1, pp. 247–270, 2020.

[15] L. Paull, S. Saeedi, M. Seto, and H. Li, "Auv navigation and localization: A review," *IEEE Journal of Oceanic Engineering*, vol. 39, no. 1, pp. 131–149, 2014.

[16] E. K. Jørgensen, T. I. Fossen, T. H. Bryne, and I. Schjølberg, "Underwater position and attitude estimation using acoustic, inertial, and depth measurements," *IEEE Journal of Oceanic Engineering*, vol. 45, no. 4, pp. 1450–1465, 2020.

[17] R. Costanzi, F. Fanelli, E. Meli, A. Ridolfi, A. Caiti, and B. Allotta, "Ukf-based navigation system for auvs: Online experimental validation," *IEEE Journal of Oceanic Engineering*, vol. 44, no. 3, pp. 633–641, 2019.

[18] E. Skjellaug, E. F. Brekke, and A. Stahl, "Feature-based laser odometry for autonomous surface vehicles utilizing the point cloud library," in *International Conference on Information Fusion (FUSION)*, 2020.

[19] M. R. U. Saputra, A. Markham, and N. Trigoni, "Visual slam and structure from motion in dynamic environments: A survey," *ACM Comput. Surv.*, vol. 51, no. 2, 2018.

[20] S. Gezici, Z. Tian, G. Giannakis, H. Kobayashi, A. Molisch, H. Poor, and Z. Sahinoglu, "Localization via ultra-wideband radios: a look at positioning aspects for future sensor networks," *IEEE Signal Processing Magazine*, vol. 22, no. 4, pp. 70–84, 2005.

[21] A. Alarifi, A. Al-Salman, M. Alsaleh, A. Alnafessah, S. Al-Hadhrami, M. A. Al-Ammar, and H. S. Al-Khalifa, "Ultra wideband indoor positioning technologies: Analysis and recent advances," *Sensors*, vol. 16, no. 5, p. 707, 2016.

[22] E. Fresk, K. Ödmark, and G. Nikolakopoulos, "Ultra wideband enabled inertial odometry for generic localization," *IFAC-PapersOnLine, 20th IFAC World Congress*, vol. 50, no. 1, pp. 11 465–11 472, 2017.

[23] K. Guo, X. Li, and L. Xie, "Ultra-wideband and odometry-based cooperative relative localization with application to multi-uav formation control," *IEEE transactions on cybernetics*, vol. 50, no. 6, pp. 2590–2603, 2019.

[24] F. Lazzari, A. Buffi, P. Nepa, and S. Lazzari, "Numerical investigation of an uwb localization technique for unmanned aerial vehicles in outdoor scenarios," *IEEE Sensors Journal*, vol. 17, no. 9, pp. 2896–2903, 2017.

[25] K. Guo, Z. Qiu, C. Miao, A. H. Zaini, C.-L. Chen, W. Meng, and L. Xie, "Ultra-wideband-based localization for quadcopter navigation," *Unmanned Systems*, vol. 04, no. 01, pp. 23–34, 2016.

[26] M. Strohmeier, T. Walter, J. Rothe, and S. Montenegro, "Ultra-wideband based pose estimation for small unmanned aerial vehicles," *IEEE Access*, vol. 6, pp. 57 526–57 535, 2018.

[27] K. Cisek, K. Gryte, T. H. Bryne, and T. A. Johansen, "Aided inertial navigation of small unmanned aerial vehicles using an ultra-wideband real time localization system," in *2018 IEEE Aerospace Conference*, 2018.

[28] J. L. Crassidis, F. L. Markley, and Y. Cheng, "Survey of nonlinear attitude estimation methods," *Journal of guidance, control, and dynamics*, vol. 30, no. 1, pp. 12–28, 2007.

[29] Y. Zhou, J. Li, and L. Lamont, "Multilateration localization in the presence of anchor location uncertainties," in *IEEE Global Communications Conference (GLOBECOM)*, 2012, pp. 309–314.

[30] F. L. Markley, "Attitude error representations for kalman filtering," *Journal of guidance, control, and dynamics*, vol. 26, no. 2, pp. 311–317, 2003.

[31] J. Sola, "Quaternion kinematics for the error-state kf," 2017, last accessed 2021-05-19. [Online]. Available: http://www.iri.upc.edu/people/jsola/JoanSola/objectes/notes/kinematics.pdf

[32] C. Van Loan, "Computing integrals involving the matrix exponential," *IEEE transactions on automatic control*, vol. 23, no. 3, pp. 395–404, 1978.

[33] ADIS 16490 - Analog Devices, 2021, last accessed 2021-05-18. [Online]. Available: https://www.analog.com/en/products/adis16490.html#

[34] NEO-M8T - ublox, 2021, last accessed 2021-05-18. [Online]. Available: https://www.u-blox.com/en/product/neolea-m8t-series